

Atomistic pseudopotential calculations of thickness-fluctuation GaAs quantum dots

Jun-Wei Luo,¹ Gabriel Bester,² and Alex Zunger¹

¹National Renewable Energy Laboratory, Golden, Colorado 80401, USA

²Max-Planck-Institut für Festkörperforschung, D-70569 Stuttgart, Germany

(Received 18 September 2008; revised manuscript received 1 December 2008; published 31 March 2009)

We calculate the electronic and optical properties of thickness-fluctuation quantum dots of different sizes and elongations using an atomistic empirical pseudopotential approach and configuration interaction. The carriers are confined by a monolayer fluctuation in the thickness of a GaAs/Al_{0.3}Ga_{0.7}As quantum well with a nominal thickness between 10 and 20 monolayers. For 10 monolayer thickness, we find several confined electron and hole levels of dominant heavy-hole character penetrating deep into the barrier (out of plane) and far beyond the physical dimension of the monolayer step (in-plane). The spatial extent of the states is strongly affected by the random-alloy fluctuations of the barrier, pushing the states toward Ga-rich regions of the interface. The similarity in the spatial extent of the electron and hole states leads to strong oscillator strength and a rich optical spectrum. The exciton as well as biexciton and trions (positive and negative) all show several lines in absorption despite the very shallow confinement potential given in these structures. The effects of correlations is drastic on the optical spectrum with the creation of highly correlated states that deviate strongly from the uncorrelated results.

DOI: 10.1103/PhysRevB.79.125329

PACS number(s): 78.67.-n, 68.65.Hb, 71.35.Pq

I. INTRODUCTION

The presence of electrons and holes in quantum-confined semiconductors leads to interesting effects different from the ones known from macroscopic systems. The potential for development seen in these nanoscopic structures has triggered a worldwide effort toward understanding the underlying physics and harnessing their properties to create new types of devices. Different realizations of semiconductor nanostructures have become popular. Especially colloidal and self-assembled quantum dots have been in the focus of attention in the last decade and, for instance, effects of particle correlation could be revealed in their optical properties as well as in their exotic charging patterns. While the thickness-fluctuation quantum dots (TFQDs) (or *natural* quantum dots) have been first realized and characterized¹⁻⁴ at about the same time as self-assembled quantum dots, only few groups have devoted their attention to them. The TFQDs are created by a monolayer (ML) fluctuation in the width of a quantum well. One of the drawback of such an approach might be the lack of control over the growth of such a step, but one of their advantages—that seem to bring about a recent revival of these structures—is their outstanding optical brightness.^{5,6} As stated, the available literature on TFQDs is scarce compared to the case of self-assembled or colloidal nanostructure. Nevertheless, a steady progress has to be acknowledged with several important milestones such as the measurement of the exciton fine structure⁷ as early as 1996 closely followed by the first calculations of the effect.^{8,9} Then followed the measurements of the biexciton,¹⁰ the characterization with near field techniques,¹¹ the optical measurements of the electron and nuclear-spin interaction,¹² the measurements of the charged excitons under magnetic field,¹³ the measurement of the biexciton decoherence rate,¹⁴ the investigations of single-photon emission,¹⁵ the near field mapping of the exciton and biexciton,¹⁶ the optical pumping of nuclear spins,¹⁷ the study of a pair of TFQDs,¹⁸ and the optical measurement of the spin.¹⁹

From the theoretical side the work was entirely within the envelope function approximation,^{8,9,20-23} which represented a natural choice since the number of atoms required is rather large and an atomistic treatment might seem prohibitive. However, the bare number of atoms is only a poor indicator for the necessity of an atomistic treatment. Indeed, the TFQD have a large extent of up to 100 nm in lateral direction but are only 3 nm thick so that the interface between the barrier and the dot will play a significant role. Also the confinement in-plane is very shallow and given by yet another atomistic feature: the monolayer step. In this paper, we will study TFQDs within the atomistic empirical pseudopotential approach. In this approach the confining potential is a consequence of the input geometry rather than an input to the calculations.

We perform calculations for four different dot sizes with lateral dimensions in nm (20,20) (40,20), (40,40), (100,20), where the elongation is along the $[1\bar{1}0]$ direction and six different well widths between 10 and 20 MLs. The number of confined electron i and hole j states (i,j) in the 10 ML-thick structure is predicted to be (1,1), (2,2), (4,4), (4,4) for the four different sizes considered. With increasing well thickness, the confinement potential becomes increasingly shallow, and for a 20 ML well width we obtain no confined states, even for the largest considered dot. We find that the alloy fluctuations within the barrier influence significantly the extent of the electron and the hole states of the TFQDs, demonstrating the penetration of the dot states into the barrier. The character of all the confined hole states is dominant heavy hole ($\approx 97\%$) with only very small light-hole (lh) contributions. This is not *a priori* expected but a consequence of vertical and lateral extent of the wave functions. A single-band treatment of these states is therefore justified from the point of view of band coupling. We find electron and hole states with very similar overall extent leading to strong optical transitions between same index states ($e_0-h_0, e_1-h_1, e_2-h_2, \dots$). The calculated optical spectrum of

TFQDs is rich, presenting several bright lines within only few meV. From the comparison of calculations at the uncorrelated and at the correlated level (configuration interaction), we can illustrate the drastic effect of correlations where the new many-body states and their optical spectrum have nothing in common with the single-particle picture. Correlations lead to a three meV redshift and an overall simplification of the optical signature.

II. METHOD OF CALCULATION

The calculation of the optical properties can be divided into two steps. In the first step, the quasiparticle wave functions are calculated using an empirical pseudopotential technique and in the second step the excitation is treated by using a configuration-interaction approach.

A. Single-particle step

In this first step we solve the single-particle Schrödinger equation for the Hamiltonian

$$\hat{H} = -\frac{\beta}{2}\nabla^2 + \sum_{n\alpha} [v_\alpha(\mathbf{r} - \mathbf{R}_n) + \hat{v}_\alpha^{\text{SO}}], \quad (1)$$

where n is an atomic index and α specifies the atom type. The Hamiltonian includes a rescaled kinetic-energy part (first term), an empirical pseudopotential part (second term), and a nonlocal spin-orbit term (last term). The screened atomic pseudopotentials v_α (with $\alpha = \text{Ga, In, As, ...}$) are centered around the locally relaxed atomic positions \mathbf{R}_n . The atomic relaxation is performed using the valence force field method to minimize the strain energy.^{24,25} The empirical atomic pseudopotentials v_α are fit in reciprocal space to accurately reproduce the electronic band structure, the electron effective mass, the heavy-hole (hh) effective masses along the [100] and [111] directions, the light-hole effective masses, the spin-orbit splittings at the Γ_{15v} and L_{1v} points, and the hydrostatic and biaxial deformation potentials. The used target values and the obtained results as well as the derived parameters are reported in the Appendix. The empirical pseudopotentials $v_\alpha(G)$ has an explicit dependence on the local hydrostatic strain, $Tr(\epsilon)$. This dependence is crucial to obtain a correct description of the volume deformation potentials.^{25,26} The spin-orbit interaction $\hat{v}_\alpha^{\text{SO}}$ is implemented in \mathbf{G} space as described in Ref. 25.

Once the total potential $\sum_{n\alpha} [v_\alpha(\mathbf{r} - \mathbf{R}_n) + \hat{v}_\alpha^{\text{SO}}]$ is defined, the eigenvalue problem is solved in a basis of strain-dependent Bloch functions $\psi_i = \sum_{n,\mathbf{k}} A_{n,\mathbf{k}} \varphi_{n,\mathbf{k}}(r)$ of band index n and wave vector \mathbf{k} of the underlying bulk solids. In this ‘‘linear combination of bulk bands’’ (LCBB) approach,²⁷ basis functions can be obtained throughout the Brillouin zone and differ in this respect from the $\mathbf{k} \cdot \mathbf{p}$ method. In the present case we exclude the Bloch states coming from X and L valleys because the intervalley coupling is negligible in the current systems, which has been tested. The current LCBB basis set consists of the bulk Bloch functions of the four bulk valence bands and the lowest conduction band. The k points are distributed around the Γ point within an ellipsoid with axis dimensions $(6/D_x, 6/D_y, 12/D_z)2\pi$, where D_x, D_y , and

D_z are the supercell dimensions. This approach incorporates naturally both intervalley (e.g., Γ - X - L) and multiband (various n 's) couplings. The ladder of electron (hole) single-particle states will be denoted as e_0, e_1, e_2, \dots (h_0, h_1, h_2, \dots).

B. Many-body step

After the single-particle eigensolutions ψ_i are obtained, the configuration-interaction (CI) method^{28,29} is used to obtain the many-body states. A set of Slater determinants $|\Phi\rangle$ is constructed from the antisymmetrized product of the single-particle wave functions. This basis set is used to expand the many-body wave functions with quantum number α for N particles $|\Psi_N^\alpha\rangle$,

$$|\Psi_N^\alpha\rangle = \sum_{a,b,c,\dots} C_{a,b,c,\dots}^\alpha |\Phi_{a,b,c,\dots}\rangle. \quad (2)$$

The indexes a, b, c, \dots run over all the different states of the particles $1, 2, 3, \dots, N$ included in the expansion. For thickness-fluctuation quantum dots, all the confined electron and hole levels are taken in the expansion. The matrix elements of the many-body Hamiltonian involves the calculation of the two center integrals for particle a and particle b

$$\begin{aligned} & \langle \psi_i^a \psi_j^b | \hat{U} | \psi_{i'}^b \psi_{j'}^a \rangle \\ &= \int \int \psi_i^*(\mathbf{r}_a) \psi_j^*(\mathbf{r}_b) v(\mathbf{r}_a, \mathbf{r}_b) \psi_{i'}(\mathbf{r}_b) \psi_{j'}(\mathbf{r}_a) d\mathbf{r}_a d\mathbf{r}_b. \end{aligned} \quad (3)$$

The screening function $v(\mathbf{r}_a, \mathbf{r}_b)$ is calculated using the model of Resta.³⁰

III. SIMULATED STRUCTURES

The *thickness-fluctuation quantum dots* or *natural dots* are, for the large majority of experiments, created by a ML fluctuation in the thickness of a GaAs quantum well surrounded by an $\text{Al}_{0.3}\text{Ga}_{0.7}\text{As}$ barrier. The structure is grown along the [001] direction and the monolayer fluctuation is achieved by growth interruption. We therefore model the structure as shown in Fig. 1 as a GaAs quantum well (blue in Fig. 1) with a nominal thickness varying between $n=10$ and 20 MLs and a 1 ML step (green in Fig. 1) locally increasing the thickness of the well between 11 and 21 MLs, respectively. The region where the dot is thicker (e.g., 11 ML instead of 10 ML) represents the quantum dot. The barrier material is assumed to be a homogeneous (without segregation) random alloy of $\text{Al}_{0.3}\text{Ga}_{0.7}\text{As}$. The simulation cells contains between 1.3 million and 4.6 million atoms. The lattice constant of GaAs (5.653 Å at $T=0$) and AlAs (5.661 Å at $T=0$) being similar, the structure is only slightly strained, compared to the typical self-assembled quantum dots grown by the Stranskii-Krastanov method.^{31,32} For the lateral dimensions of the step (L_x, L_y) , along the $[1\bar{1}0]$ and the $[110]$ directions, respectively, we have selected four different length-width combinations $(L_x, L_y) = (20, 20), (40, 20), (40, 40)$, and $(100, 20)$, given in nm. These sizes have been chosen in accordance with the literature^{4,7,16,33-35} where elon-

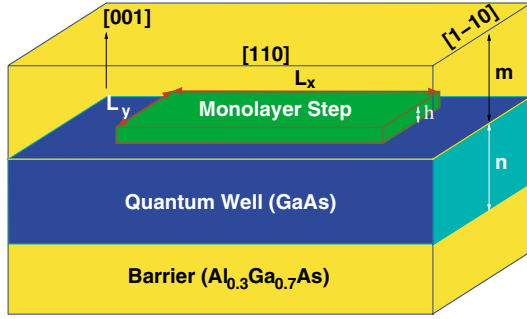


FIG. 1. (Color online) Schematic representation of the simulated structures for the thickness-fluctuation quantum dots (TFQDs). The monolayer step is shown in green on top of the GaAs quantum well with thickness n , shown in blue. The $\text{Al}_{0.3}\text{Ga}_{0.7}\text{As}$ barrier is shown in yellow. The elongation of the monolayer step is along the $[1\bar{1}0]$ direction.

gations along the $[1\bar{1}0]$ direction have been reported.

IV. RESULTS FOR QUANTUM WELLS

Before we address the results for the thickness-fluctuation quantum dots we performed calculations on $\text{GaAs}/\text{Al}_{0.3}\text{Ga}_{0.7}\text{As}$ quantum wells. The purpose of these calculations is twofold. One is testing of the empirical pseudopotentials for GaAs and AlAs (a detailed description of these potentials can be found in the Appendix) in a nanostructure setting and for a random alloy of $\text{Al}_{0.3}\text{Ga}_{0.7}\text{As}$. The second is to illustrate the magnitude of the potential confinement originating from a monolayer difference in the quantum-well thickness.

We have calculated the valence-band maximum (VBM) and the conduction-band minimum (CBM) for $(\text{GaAs})_n/(\text{Al}_{0.3}\text{Ga}_{0.7}\text{As})_{40-n}$ superlattices. The number n refers to the number of MLs in the GaAs quantum well. The sum of the quantum well and the barrier MLs is 40, and is kept constant. In Fig. 2 the single-particle results for the $(\text{GaAs})_n/(\text{Al}_{0.3}\text{Ga}_{0.7}\text{As})_{40-n}$ superlattice are summarized. The energies of the CBM and VBM are given as stepped red line and as a blue line going through the center of each of the steps. The energies are given as a function of the quantum-well thicknesses in units of monolayers. The numbers above each step gives the energy difference for VBM and CBM between to adjacent thicknesses in meV. These numbers are most relevant for the TFQDs since they give the depth of the confinement potential for the carriers. For instance, for a quantum well with a nominal 15 ML thickness and a one ML fluctuation (the well is locally 16 ML thick) the confinement potential for electrons and holes is 7.1 and 2.0 meV, respectively. Experimentally determined ground excitonic PL energies (Gammon,⁷ Erdmann,³⁶ Rudra,³⁷ Courboules,³⁸ Brunner²) are shown as filled symbols and lie around 10 meV below the theoretical single-particle band gaps given by the green line and symbols. This difference can be explained by electron-hole Coulomb interaction neglected in the calculations at this stage. The agreement between theory and experiment is very good. The theoretical results can be fitted by the functions

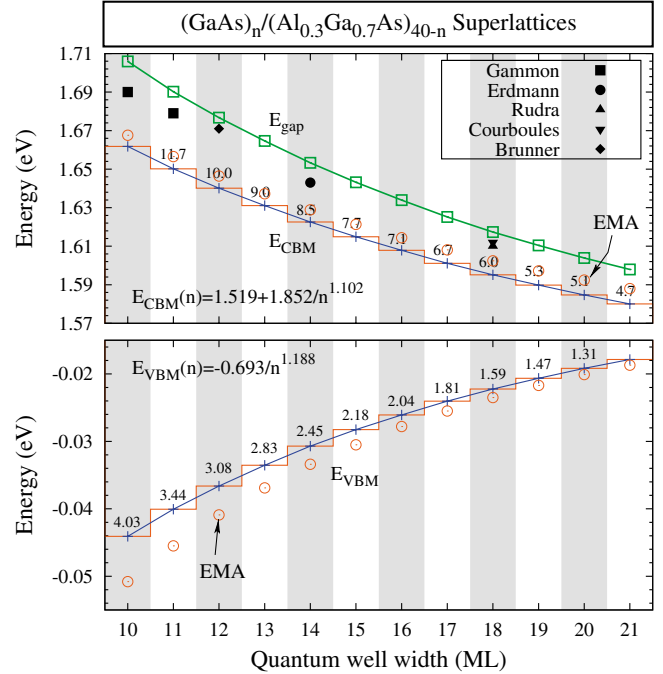


FIG. 2. (Color online) Energies of the CBM and VBM of a GaAs quantum well in $\text{Al}_{0.3}\text{Ga}_{0.7}\text{As}$ as a function of quantum-well width in units of monolayers. The empirical pseudopotential results are given as blue and red lines. The numbers above each step gives the energy difference for VBM and CBM between to adjacent thicknesses in meV. Experimental ground excitonic PL energies are extracted from the literatures [Gammon (Ref. 7), Erdmann (Ref. 36), Rudra (Ref. 37), Courboules (Ref. 38), Brunner (Ref. 2)] and given as filled symbols. The calculated single-particle band gap (difference between CBM and VBM) is given as green line. The effective-mass results from Eq. (6) are given as red circles.

$$E_{\text{CBM}}(n) = 1.519 + 1.852/n^{1.102}, \quad (4)$$

$$E_{\text{VBM}}(n) = -0.693/n^{1.188}, \quad (5)$$

where the VBM of GaAs has been chosen as energy reference. The effective-mass solution for a particle with effective mass m^* which is subject to a potential energy $V_b(z)$ such that it has the value 0 for $|z| > L/2$ and $-V_b$ for $|z| < L/2$, where L is the thickness of the potential well is given by the transcendental equation³⁹

$$k_w \tan\left(k_w \frac{L}{2}\right) = \kappa_b \quad (6)$$

with $k_w = \sqrt{\frac{2m^*}{\hbar^2}(E + V_b)}$ and $\kappa_b = \sqrt{-\frac{2m^*E}{\hbar^2}}$.

Using the parameters $V_b(\text{electron}) = 0.264$ eV, $V_b(\text{hole}) = 0.151$ eV, $m_e^* = 0.067$, and $m_h^* = 0.34$ the agreement with the empirical pseudopotential calculations is very good throughout the range of thicknesses for the conduction-band states. For the valence-band states, some deviations for thinner quantum wells in the case of the valence-band states can be attributed to the increasing importance of the barrier. We find that the heavy-light-hole coupling for the zone-center states increases with decreasing GaAs well thickness.

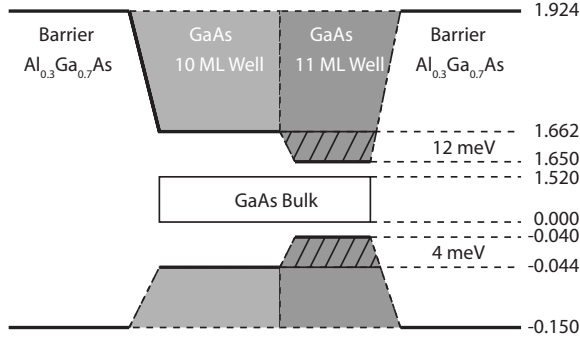


FIG. 3. Schematic representation (not to scale) of the band edges of the thickness-fluctuation quantum dots. The numbers are given in eV, unless specified. The hatched region describes the energetic window where states can be confined in all three dimensions.

V. CONFINEMENT POTENTIAL

In Fig. 3 we schematically illustrate the band edges of the materials involved in the TFQD. The reference energy is set to zero for the GaAs bulk VBM. The alloy barrier has conduction and valence-band edges at 1.924 and -0.150 eV, respectively. For the quantum well with 10 ML thickness, the conduction- and valence-band edges are at 1.662 and -0.044 eV, respectively. These numbers change to 1.650

and -0.040 eV for the 11 ML well. The hatched region in the Fig. 3 highlights the potential drop responsible for the confinement of electrons and holes in a TFQD with 10 ML nominal thickness. The electrons and holes are confined by only 12 and 4 meV, respectively. Only states within this energetic window can be confined in all three directions. Conduction (valence) -band states with energy between 1.662 and 1.924 eV (-0.044 and -0.150 eV) are quantum-well states confined in [001] direction but dispersive in-plane. Compared to the case of self-assembled InGaAs dots in GaAs with electron and hole confinement potentials of up to hundreds of meV, the situation is drastically different. Based on this qualitative analysis we expect states that tend to leak from the 11 ML dot region to the well region with 10 ML.

VI. SINGLE-PARTICLE ENERGIES FOR DIFFERENT LATERAL DIMENSIONS

The summary of the single-particle energies for a TFQD with 10 ML nominal well thickness is given in Fig. 4. The band edges of the alloy $\text{Al}_{0.3}\text{Ga}_{0.7}\text{As}$ are given as blue lines and the confinement potential for the TFQD states as red lines. As stated above these represent the band edges of 10 and 11 ML GaAs quantum wells. The obtained single-particle eigenvalues are given as black lines and are labeled as e_0 , e_1 , and e_2 for the electron states and h_0 , h_1 , h_2 , h_3 , and

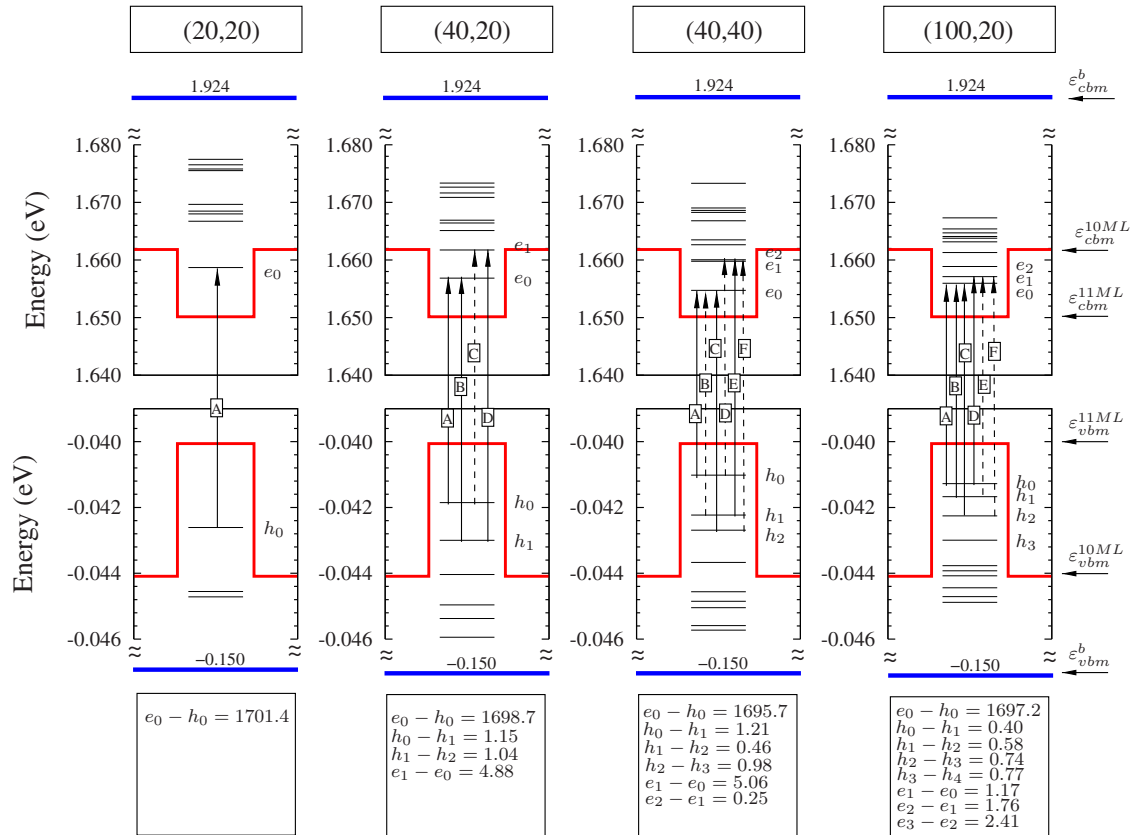


FIG. 4. (Color online) Single-particle energy levels of $(\text{GaAs})_n/(\text{Al}_{0.3}\text{Ga}_{0.7}\text{A})_{40-n}$ monolayer thickness-fluctuation quantum dots with well width of $n=10$ ML and lateral base size (L_x, L_y) of (20,20), (40,20), (40,40), and (100,20) nm, respectively. The red lines indicate the energy edges of the quantum well with width of 10, and 11 MLs. The reference energy is set to zero for the $\epsilon(\Gamma_{15v})$ level of bulk GaAs. Blue lines given the energy edges of $\text{Al}_{0.3}\text{Ga}_{0.7}\text{As}$ barrier. The arrows show some of the possible excitonic transitions.

\hbar_4 for the hole states. The smallest (20,20) TFQD has only one confined electron and one confined hole state while for the largest (100,20) TFQD four electron and four holes states are confined. The “shell structure,” known from self-assembled quantum dots where the levels are grouped in *S*, *P*, *D* shells with degeneracy of 1,2,3, respectively, can be perceived for the (40,40) TFQD. However, for the smaller dots where only one level is confined and for the elongated dots there is no obvious pattern in the level spacings. The magnitude of the level spacings is an order of magnitude smaller than in self-assembled or colloidal quantum dots. The spacing between the first and second electron (hole) states in the (40,40) TFQD is only 5 (1) meV.

This can be seen as surprising, since the dimension of the TFQD is not very different than for some self-assembled quantum dots [e.g., 40 nm diameter and 3 nm height InGaAs/GaAsP dots grown by MOVPE (Ref. 40) are very similar in size to our (40,40) TFQD]. The reason for this qualitative difference is due to mainly two effects: (i) The small in-plane confinement potential given in TFQD allowing wave functions to leak out much more than in self-assembled quantum dots leading to wave functions with a much larger extent; (ii) The electron effective mass of GaAs is with 0.067 almost three times larger than for InAs 0.023 leading to a smaller level spacing in TFQDs. Argument (i) of the penetration of wave function holds for holes but not argument (ii) since the hole effective masses of InAs and GaAs are similar. We will present a further argument for holes in Sec. IX

VII. SINGLE PARTICLE ENERGIES FOR VARYING WELL THICKNESS

In Fig. 5 we show the calculated single-particle electron and hole energies for TFQDs with varying quantum-well width between 10 and 20 monolayers. The TFQDs have a lateral base size (L_x, L_y) of (100,20) nm. The reference energies for the electron states are set to the CBM of the quantum wells with width $N+1$ monolayers. Respectively, the reference energies for the hole states are set to the VBM of the quantum wells with width $N+1$ monolayers. The absolute values of the CBM and VBM of the quantum wells as a function of well width have been reported in Fig. 2. The shaded areas, in Fig. 5, delimit the states that experience three-dimensional (3D) confinement (confined in the dot) from the ones experiencing only one-dimensional (1D) confinement (confined inside the well). For a TFQD grown on a 12 ML thick quantum well, three electrons states and four hole states are confined. When the thickness of the well increases, the confinement potential decreases, as was discussed in Sec. IV. This is shown by the black lines approaching zero with increasing well width. In contrast, the confinement energies of the electron and hole states shown in Fig. 5 exhibit almost no dependence on the well width. This shows that the electron and hole states move almost rigidly with the CBM and VBM of the quantum well. This effect leads to the counterintuitive result that when the volume of the dot becomes larger (the well thickness is increased) the number of confined states is reduced. We conclude that in order to have 3D confined states, the well width should be

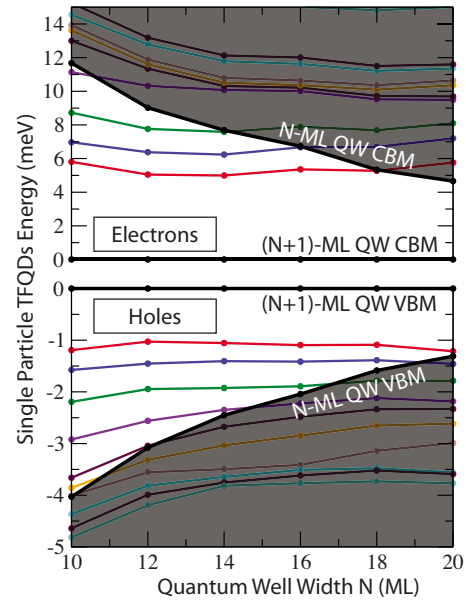


FIG. 5. (Color online) Single-particle energy levels of TFQDs with lateral base size (L_x, L_y) of (100,20) nm and varying quantum-well width N , where N is the number of monolayers. The reference energy for the electrons (holes) is set to zero for the conduction (valence) band minimum (maximum) of the quantum well with $N+1$ monolayers.

smaller than 20ML or the lateral dimensions of the TFQD must be larger than the 100×20 nm² we assumed here.

VIII. SINGLE-PARTICLE WAVE FUNCTIONS

Some of the aspects discussed previously based on the band edges of the TFQD can be recognized by looking at the single-particle wave functions. In Fig. 6 we plotted the square of the first two electron and first two hole wave functions for the (40,20) TFQD with 10 ML nominal well thickness. The dot is shown as a light gray transparent parallelepiped; it shows not only the 1 ML step but delimits the space region where the quantum well is 11 ML thick. The value used for the green isosurface is half of the maximum of the squared states. The magenta (cyan) colored line gives the value of the squared wave functions along the [100] ([001]) direction through the dot region where the states are mostly localized (indicated by cyan and magenta lines in the isosurface plots). The supercell dimension is $57 \times 57 \times 11$ nm³ and the abscissa of the line plots is normalized so that the cyan line spans the [001] direction from 0 to 11 nm and the magenta line the [100] direction from 0 to 56 nm. While it can also be seen from the line plots that the states are well confined within the simulation cell, we notice that the states occupy a large fraction of the supercell to decay to zero only close the cell boundary. From the plots we learn that the consequence of the shallow confinement potential in-plane allows the wave function to penetrate significantly into the barrier. The out-of-plane (along [001]) confinement is stronger since it is given by the band offset between GaAs and the Al_{0.3}Ga_{0.7}As barrier (see Fig. 3) but the 3 nm well is thin

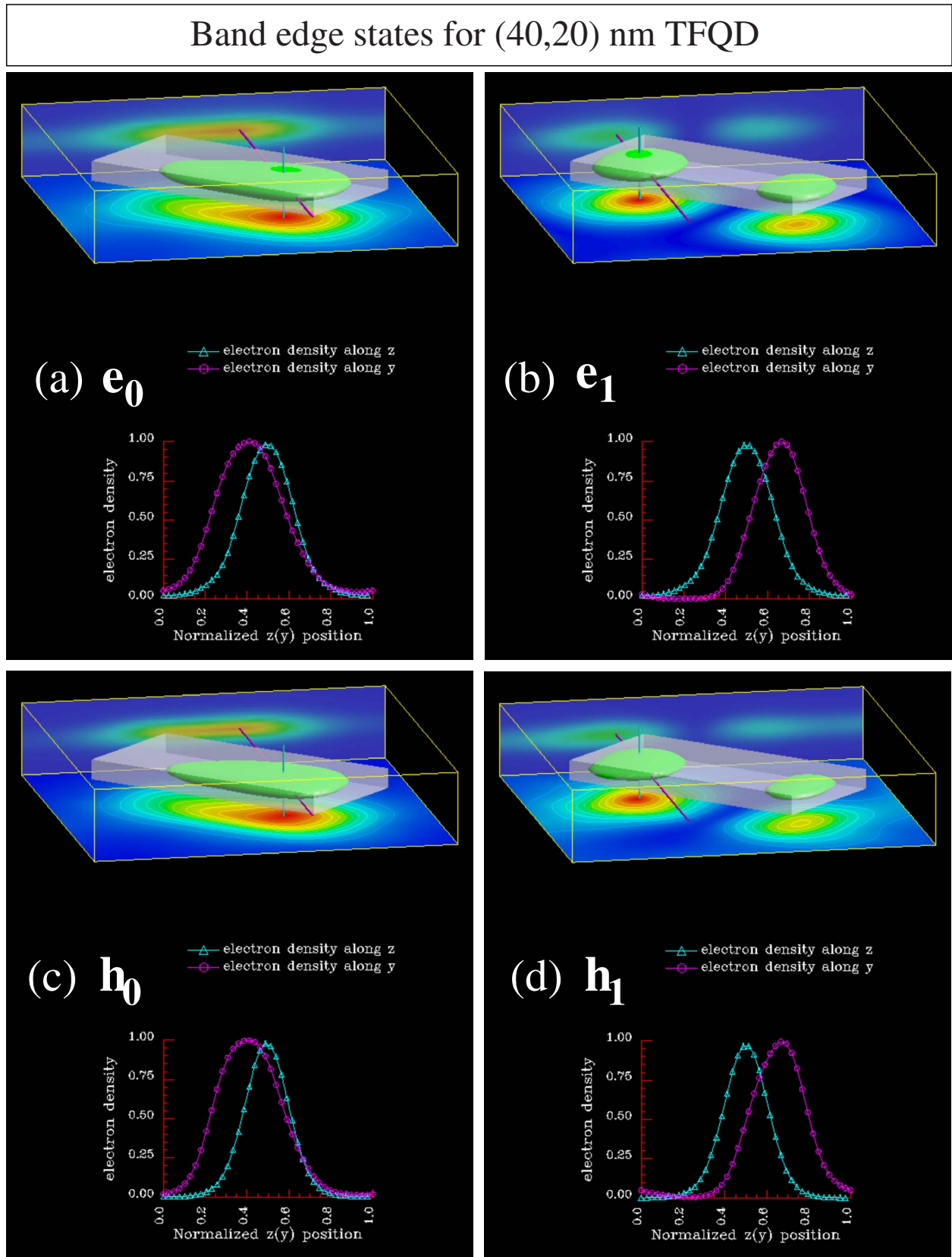


FIG. 6. (Color online) Squares of the real-space wave functions of the lowest two electron (e_0, e_1) and highest two hole states (h_0, h_1) for a $(\text{GaAs})_{10}/(\text{Al}_{0.3}\text{Ga}_{0.7}\text{As})_{30}$ TFQD with lateral size of $(40, 20) \text{ nm}^2$. The line plots represent the wave functions squared along two lines parallel to the $[100]$ (magenta) and the $[001]$ directions (cyan).

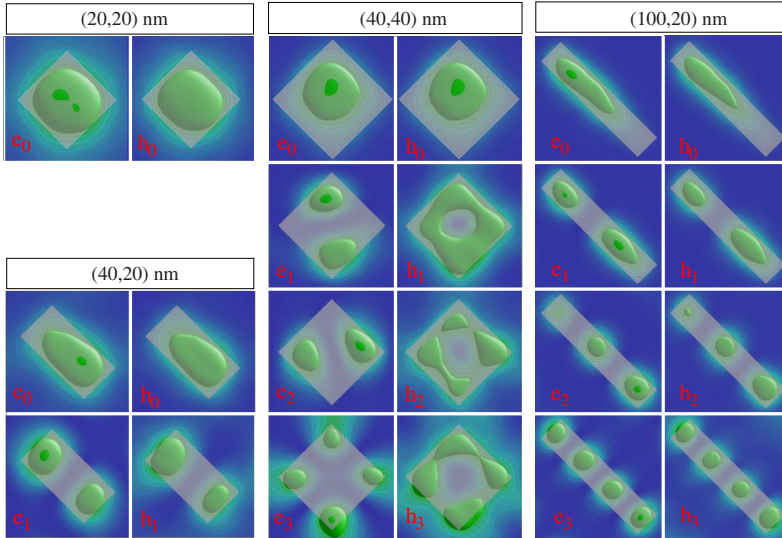


FIG. 7. (Color online) Squares of the real-space wave functions for the lowest electron and highest hole states for $(\text{GaAs})_{10}/(\text{Al}_{0.3}\text{Ga}_{0.7}\text{As})_{30}$ TFQD with lateral sizes of (20,20), (40,20), (40,40), and (100,20) nm^2 . The gray rectangles indicate the position and shape of the TFQD.

enough to lead to significant wave-function leakage into the $\text{Al}_{0.3}\text{Ga}_{0.7}\text{As}$ barrier.

This penetration of wave function into the barrier can be directly witnessed by the in-plane asymmetric shape of the isosurfaces: the *S*-like states e_0 and h_0 are pushed toward one side of the dot and the *P*-like e_1 and h_1 toward the other side. These asymmetries are caused by the random nature of the $\text{Al}_{0.3}\text{Ga}_{0.7}\text{As}$ barrier alloy that favors wave-function penetration into locally Ga-rich (Al-poor) regions where the barrier is lower.

In Fig. 7 we summarize the results of the confined states of the (20,20), (40,20), (40,40), and (100,20) nm^2 TFQD as a top view of the squares of the real-space wave functions. We notice a striking similarity between the electron and the hole states and a progression that corresponds to an increase in the number of nodes of the wave functions, as expected from a single-band wave function. The *P*-like states of the (40,40) nm^2 are oriented along the corners of the dot along [100] and [010] unlike self-assembled InGaAs quantum dots where the [110] and [1 $\bar{1}$ 0] directions are preferred. From the similar localization behavior of the e_0 and h_0 states we can expect a strong oscillator strength for the e_0 - h_0 transition.

IX. SYMMETRY ANALYSIS

The fact that the material system $\text{GaAs}/\text{Al}_{0.3}\text{Ga}_{0.7}\text{As}$ is mostly unstrained leads *a priori* to a situation very different to the one present in heavily strained self-assembled InGaAs quantum dots. In the latter case the strong biaxial strain leads to a large splitting of the heavy- and light-hole bands, leaving the heavy-hole band as the VBM. In the present case of TFQD no such strain-driven splitting is expected and the VBM of GaAs is of Γ_8 symmetry with degenerate heavy- and light-hole bands. In the case of a quantum well, the confinement splits the heavy from the light-hole band by about 15 meV for a 10 nm thick GaAs QW in $\text{Al}_{0.3}\text{Ga}_{0.7}\text{As}$ at the $\bar{\Gamma}$ point.³⁹ The confinement in-plane leads to folding of the dispersive QW bands toward $\bar{\Gamma}$ and to the mixing of the heavy- and light-hole bands. To analyze the symmetry char-

acter of the TFQD states we project them onto bulk GaAs Γ -point Bloch states and construct the hh, lh, and split-off (so) combinations.⁴¹ The results for hole states are summarized in Table I where the percentage of the hh, lh, and so contributions are tabulated along with the energy of the states relative to the GaAs VBM. We see that all the states are strongly dominant hh with only few percent lh character.

In Table I we also report results for two lens-shaped GaAs quantum dots embedded in $\text{Al}_{0.3}\text{Ga}_{0.7}\text{As}$. For “Lens 1” with a height (h) of 3.5 nm (very similar to the 3 nm thickness of the TFQDs) we see that the first hole state is to 86% hh, a

TABLE I. Symmetry analysis of the single-particle-hole states. The heavy-hole (hh), light-hole (lh), and split-off (so) contributions are given in percent. The energy, ε , is the single-particle energy given relative to the valence-band maximum of GaAs. The dimensions L_x , L_y and b (base diameter), h (height) are given in nm.

L_x, L_y	State	hh	lh	so	ε (meV)
(20,20)	h_0	97	2	0	42.3
(40,40)	h_0	98	1	0	40.7
	h_1	96	3	0	41.9
	h_2	97	2	0	42.4
(40,20)	h_0	97	2	0	41.6
	h_1	96	3	0	42.7
	h_2	96	3	0	43.7
(100,20)	h_0	98	1	0	41.0
	h_1	97	2	0	41.4
	h_2	97	2	0	42.0
	h_3	96	3	0	42.7
Lens 1 $b=20, h=3.5$	h_0	86	12	0	45.3
	h_1	46	53	0	51.7
	h_2	39	60	0	53.9
Lens 2 $b=20, h=10$	h_0	86	13	0	20.6
	h_1	41	58	0	21.9
	h_2	39	60	0	24.4

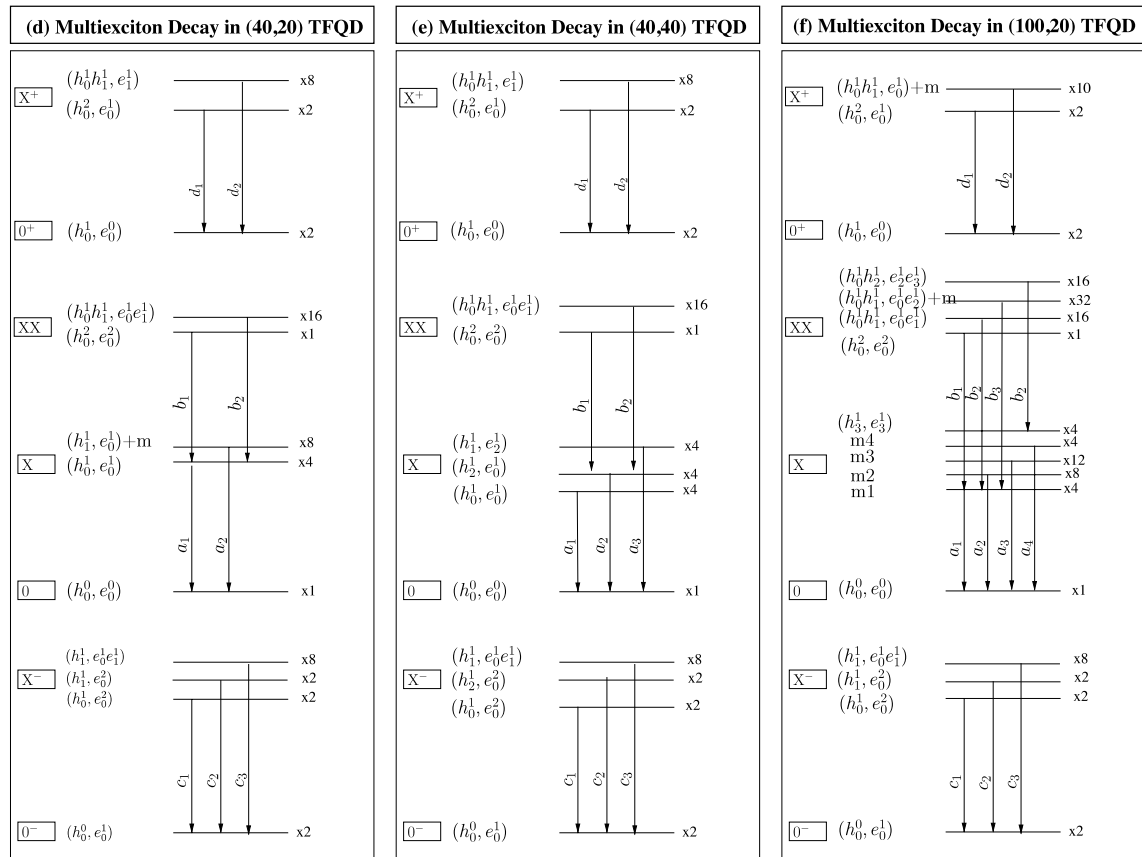
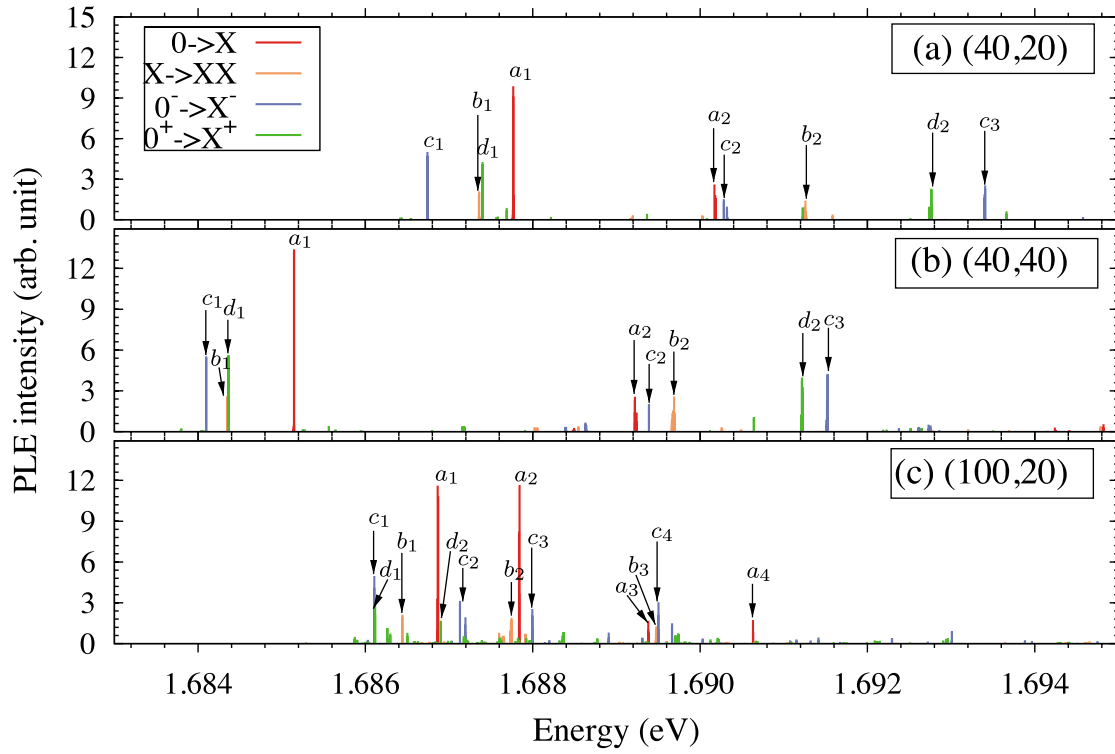


FIG. 8. (Color online) (a-c) Absorption spectra for the (40,20), (40,40), and (100,20) nm² TFQDs, including the exciton (X), the biexciton (XX), and the charged trions (X⁺, X⁻). [(d)–(f)] Schematic illustration of the leading peaks in absorption with their dominant configurations, given in parenthesis, and with the letter *m* in case the many-body state does not have a single dominant configuration.

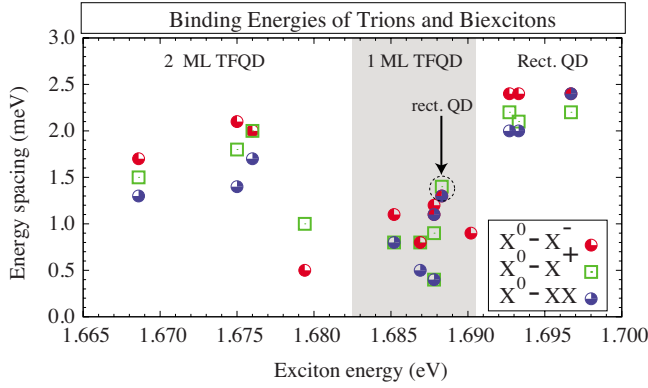


FIG. 9. (Color online) Binding energy of the trions states and of the biexciton for three types of quantum dots. For TFQDs with one ML thickness fluctuation, TFQDs with two ML thickness fluctuations and for rectangular GaAs parallelepiped with height 11 ML fully embedded in $\text{Al}_{0.3}\text{Ga}_{0.7}\text{As}$.

value significantly lower than for the (20,20) TFQD of similar dimensions. This is an additional indication that in spite of the similar sizes of the dots, the wave function occupies a significantly larger in-plane area in the case of the TFQD. The h_1 and h_2 states of Lens 1 dot are mixed hh-lh states due to the similar energetic position of h_1 , h_2 , and the light-hole band. The results for “Lens 2” quantum dot with large height (half sphere) is similar to Lens 1 case, with a hh dominant h_0 and mixed hh-lh h_1 and h_2 states, but for another reason. The large height leads to a smaller hh-lh splitting and despite the lower energetic position (around 20 meV above GaAs VBM) the hole states are energetically close to the lh band.

The calculations with the lens-shape dots illustrates the that hh-lh mixing is a consequence of (i) the lateral extent of the wave functions, controlling the energetic position of the states relative the quantum-well light-hole band, and (ii) the thickness of the well (dot, in Lens 1 and 2 cases) controlling the energetic position of the quantum-well light-hole band. For our TFQDs the large lateral extent of the wave functions

and the narrow width of the well leads to almost pure heavy-hole states.

The benefit of the atomistic approach compared to a continuum description lies in a quantitative prediction of the effects described so far: (1) Continuum models rely on an external input for the potential, historically taken as a cylindrical potential^{22,45} with certain band offsets and the results obtained are direct consequences of these assumptions. Our approach directly takes the shape of the structure as input parameter. (2) The penetration of states into the barrier is important since it governs the nature and the number of confined states, and requires the proper treatment of the interfaces and the matching of different types of Bloch functions, not given in a continuum description. (3) Another typical atomistic effect is the fact that alloy fluctuations in the barrier modify the distribution of wave functions significantly making them very much unlike the spherically symmetric wave functions commonly assumed. (4) The capability to analyze the wave functions in term of their Bloch function character gives a direct indication for the quality of a single-band approach, which may appear unfounded otherwise.

X. OPTICAL PROPERTIES

From the single-particle results we are able to calculate optical properties using the configuration-interaction approach as described in Sec. II. In our implementation only states confined within the simulation cell can be handled meaningfully. For the TFQD this represents an early truncation of the expansion of the many-body wave functions. For the (20,20) system, for instance, only one electron and one hole state can be taken into account which means that we are not going beyond the single-configuration uncorrelated level. For larger dots, as the (20,100), we take four electron and four hole states into account, and include correlations in the many-body states.

In Figs. 8(a)–8(c) we show the calculated absorption spectra for the (40,20), (40,40) and (100,20) nm^2 TFQDs,

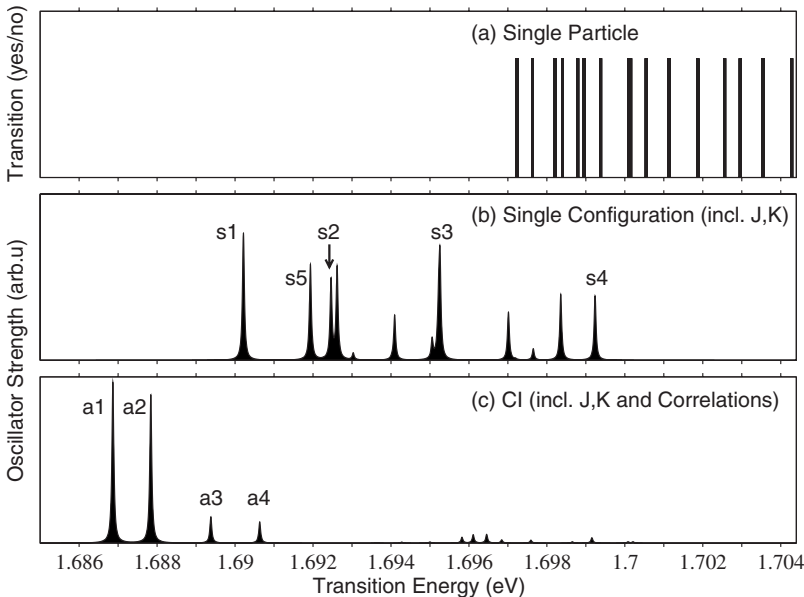


FIG. 10. Excitonic transitions for a (100,20) TFQD calculated at three levels of approximation. (a) Single-particle levels, it is only the difference between single-particle electron and hole energies are calculated. (b) Single configuration level, where the Coulomb interaction is added to each of the 4×4 configuration blocks. (c) Configuration-interaction level where correlations are included using all the available confined states.

TABLE II. Summary of the theoretical results for selected properties of $(\text{GaAs})_{10}/\text{Al}_{0.3}\text{Ga}_{0.7}\text{As}$ TFQDs with different lateral dimensions (L_x, L_y) (nm^2) and experimental results.

Property	(20,20)	(40,20)	(40,40)	(100,20)	Expt.
X^0 (eV)	1.6902	1.6878	1.6851	1.6869	1.6813 ^a , 1.6886 ^b , 1.655 ^c
X^{-1} (eV)	1.6893	1.6867	1.6841	1.6861	1.6856 ^b , 1.652 ^b
$\Delta(X^0 - X^{-1})$ (meV)	0.9	1.1	1.0	0.8	3.0 ^b
δ_0 (μeV)	8	6	4	5	~ 100 ^{b, d}
δ_b (μeV)	0	5	0	4	~ 24 ^{a, d}
δ_d (μeV)	1	7	1	0	~ 1 ^d

^aReference 7.

^bReference 13.

^cReference 45.

^dReference 12.

including the transitions from the exciton (X), the biexciton (XX), and the charged trions (X^+ , X^-). In Figs. 8(d)–8(f) we show the origin of the main transitions in the spectra [(a)–(c)] by giving the dominant configuration(s) of each level in parenthesis. We use the notation e_i^j and h_i^j where i is the index for the state and j the occupation of this state. Due to the few number of confined levels in the (20,20) TFQD (only one electron and one hole state) only few dot-to-dot transitions are possible leading to a very simple picture we omitted here. In the absorption spectra for the (40,20) and (40,40) nm^2 TFQD [Fig. 8(a) and 8(b)] we can see a group of peaks around 1.685 and 1.687 eV. These transitions involve mainly the states e_0 and h_0 as can be seen in the analysis in Figs. 8(d) and 8(e). The transitions above 1.688 eV involve the higher excited states e_1 , e_2 , h_1 , and h_2 and are well isolated from the first group of peaks. The situation is different in the case of the (100,20) nm^2 TFQD [Fig. 8(c)] where all the transitions are grouped together between 1.687 and 1.692 eV. This smaller “bandwidth” of CI states is surprising considering that we are taking the same energy window for electrons and hole states as in the (40,20) and (40,40) cases. We will discuss this effect in Sec. XI. Another general observation is that the XX, X^+ , and X^- transitions

denoted by b_1 , d_1 , and c_1 , respectively, are all redshifted with respect to the main X transition (a_1) in all calculated dots. In Fig. 9 we summarized calculations for the binding energy of the trions and biexcitons for three types of quantum dots. For TFQDs with one ML thickness fluctuation, TFQDs with two ML thickness fluctuations and for rectangular GaAs parallelepiped with height 11 ML fully embedded in $\text{Al}_{0.3}\text{Ga}_{0.7}\text{As}$. The results are plotted as a function of the exciton energy. The TFQDs with two ML thickness fluctuations have binding energies around 2 meV while it is around 1 meV for the TFQDs with 1 ML thickness fluctuations. The fully embedded quantum dots (Rect. QD) emit at higher energy and have between 2 and 2.5 meV binding energies.

For the case where no charged states are created and the excitation power is low enough to avoid the creation of biexciton, only the red lines in Figs. 8(a)–8(c) should be observed. We see two, three and four dominant peaks for the (40,20), (40,40), and (100,20), respectively. This represents a significant simplification from the single-particle picture with 16 possible transitions for the (40,40) and (100,20) TFQDs between confined states ($e_{0,1,2,3}$ and $h_{0,1,2,3}$ are confined). We will see that correlations are responsible for this simplification in Sec. XI. We note also that for the (40,40)

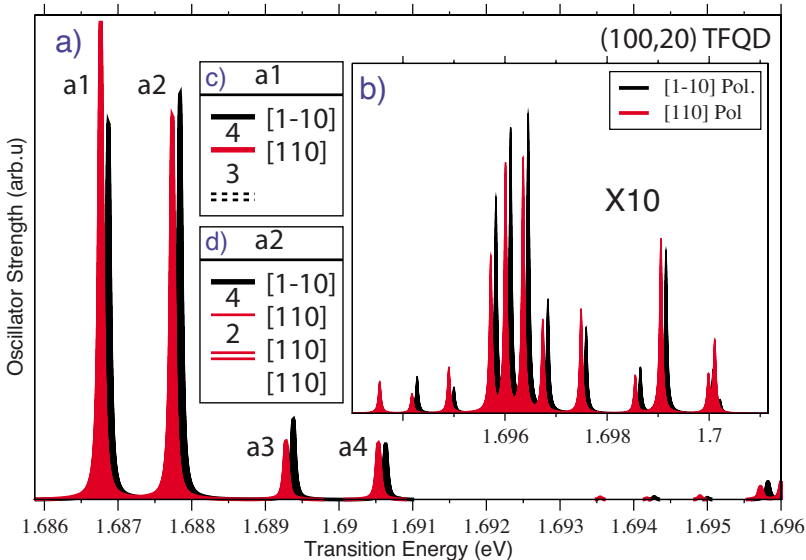


FIG. 11. (Color online) Excitonic transitions for a (100,20) TFQD calculated for the polarization direction $[110]$ and $[1\bar{1}0]$. Inset (b) shows a magnified high energy region. The $[1\bar{1}0]$ polarized spectrum has been shifted by 0.1 meV to the blue *artificially* in (a) and (b) for graphical purposes in order to see the degree of polarization. The fine structure of the peaks p1 and p2 are given in the insets (c) and (d) where numbers are given in μeV .

TABLE III. Summary of experimental results on TFQDs.

TFQDs	X^0 (eV)	$\Delta(X^0-X^{-1})$ (meV)	$\Delta(X^0-XX)$ (meV)	FS (μeV)	Note
(GaAs) ₁₀ /Al _{0.3} Ga _{0.7} As	1.6813 ^a ,	3.0 ^b	3.4 ^c	$\delta_b(E_0)=-25$ ^a ,	$\Delta(E_1-E_0)=2.5$ meV ^a
	1.6886 ^b	3.0 ^c		$\delta_b(E_1)=41$ ^a ,	$\Delta(E_2-E_1)=1.0$ meV ^a
	1.655 ^c			$\delta_b(E_2)=45$ ^a ,	$\Delta(E_3-E_2)=0.5$ meV ^a
				$\delta_b(E_3)=-22$ ^a	$\Delta(E_4-E_3)=0.5$ meV ^a
				$\delta_b(E_4)=-47$ ^a	
			$\delta_0 \sim 100$ ^{b,d} ,		
			$\delta_d \sim 1$ ^d ,		
			$\delta_b \sim 24$ ^d		
(GaAs) ₁₂ /Al _{0.35} Ga _{0.65} As	1.6586 ^c	3.2 ^c			
(GaAs) ₁₀ /Al _{0.33} Ga _{0.67} As	1.6977 ^f ,		2.7 ^f		$t_X=100$ ps ^f ,
	1.687 ^g ,		2.6 ^h		$t_{XX}=60$ ps ^f ,
	1.6988 ^h				$f=75$ ^f
(GaAs) ₁₅ /Al _{0.3} Ga _{0.7} As	1.6280 ^b	3.4 ^c			
	1.6212 ⁱ		3.36 ⁱ		
(GaAs) ₂₂ /Al _{0.3} Ga _{0.7} As	1.5936 ^b ,	3.5 ^k			NSOM ^j
	1.663 ^k				
	1.585 ^j				
(GaAs) ₃₀ /Al _{0.3} Ga _{0.7} As	1.5598 ^b				
(GaAs) ₅₀ /Al _{0.3} Ga _{0.7} As	1.5356 ^b	1.2 ^b			
(GaAs) ₁₀ /Al _{0.33} Ga _{0.67} As	1.6796		4.0 ^l		

^aReference 7.

^bReference 13.

^cReference 45.

^dReference 12.

^eReference 2.

^fReference 5.

^gReference 15.

^hReference 6.

ⁱReference 14.

^jReference 11.

^kReference 17.

^lReference 10.

dot, where the attempt to label the states as S , P , and D , might seem justified, the transition a_2 is clearly visible, despite its dominant S - P character. Transitions of that type are mostly forbidden in self-assembled quantum dots.⁴² For the negative trion, we calculate three dominant transitions for the (40,20) and (40,40) dots and seven for the (100,20) dot. For the positive trion we only see two dominant peaks for all the dot sizes. This qualitative difference emphasizes again the different nature of the electron and hole states despite the dominant single-band character of both electrons and holes.

XI. EFFECT OF CORRELATIONS

To illustrate the effect of correlations onto the optical properties of TFQDs we use the example of the excitonic transitions in the (100,20) TFQD. In Fig. 10 we present three different levels of approximation. At the first level only the single-particle energies, as given in Fig. 4, are considered. In Fig. 10(a) the resulting single-particle gaps are given as bar chart. In the next level the direct and exchange Coulomb interactions are included within each configuration 4×4 blocks. One configuration consists of the product of one single-particle electron and one single-particle-hole state leading to a 4×4 matrix when spin is included. This corre-

sponds roughly to the Hartree-Fock level,⁴³ which exactly neglects correlations. The results for the absorption at this level are given in Fig. 10(b). In the last step we include coupling between the configurations via configuration interaction where all the available confined levels are utilized. The results are given in Fig. 10(c). While this last step represents the limit of the present approach and is sometimes referred to as “full CI,” it likely misses some of the correlations.

In Fig. 10 we notice that the entire spectrum is shifted to the red when Coulomb interactions are introduced [difference between Figs. 10(a) and 10(b)]. This is expected since the electron-hole attraction in these structures extends between 0 and 7 meV, depending on the considered states. As we can expect from the extent of the wave functions (Fig. 7) the transitions between the states e_i and h_j , where the indices i and j are equal, are bright. These are labeled as $s1$ – $s4$ for e_0h_0 , e_1h_1 , e_2h_2 , and e_3h_3 , respectively. However, several other transitions lead to significant oscillator strength, as for instance e_0h_1 , labeled as $s5$ in Fig. 10(b). The inclusion of correlations leads to a dramatic modification of the spectrum [difference between Fig. 10(b) and 10(c)] where we recover the results from Figs. 8(c) and 8(f) with the four strongest peaks $a1$ – $a4$. Most of the bright transitions at the single-configuration level become dark and the states rearrange

TABLE IV. Empirical pseudopotential parameters. Ω is given in (a.u.)³ and the parameters are described in Eqs. (A1) and (A2).

	Ω	λ (so)	f (strain)	α	β	γ
AlAs						
Al	111.3	0.01521	0.60143	-1.66758E+00	1.33822E+00	0.00000E+00
		1.94543E-01	1.02429E+01	2.04603E+00		
		6.14786E-03	1.72295E+00	7.54964E-02		
		6.53510E-02	2.44440E+00	9.14389E-01		
As	145.2	0.20415	0.00000	-1.08906E+00	9.72466E-01	0.00000E+00
		1.02613E-02	6.55475E+00	5.17899E-01		
		1.10768E-01	2.94879E+01	8.16180E-01		
		1.15186E-01	1.67404E+00	1.55176E+00		
GaAs						
Ga	131.4	0.01959	0.679603	-1.41766E+00	1.29519E+00	0.00000E+00
		5.16039E-02	1.21363E+00	1.61056E+00		
		4.79699E-02	4.90228E-01	1.47962E+00		
		-3.35084E-02	6.63229E+00	2.73530E+00		
As	145.2	0.16803	0.00000	-1.08911E+00	9.66992E-01	0.00000E+00
		-1.69009E-02	5.95384E+00	2.92374E+00		
		-6.16557E-02	3.46560E+00	1.13430E+00		
		1.22540E-01	8.26516E-01	1.22483E+00		

themselves to lead to a simple spectrum, where the lowest energy transitions is shifted by a correlation energy of more than 3 meV. The analysis of the origin of the lowest energy peak *a1* shows that it is to 60% given by the e_0h_0 configuration with an admixture of 40% from several other configurations [In Fig. 8(f) we labeled this mixture as *m1*.] The second lowest peak *a2* is 36% h_1e_0 and 28% h_0e_1 with the remaining 36% contain a large number of different configurations. The inclusion of correlations leads therefore to the creation of entirely new and different states that we may call highly correlated. This is unlike the case of colloidal quantum dots, where correlations are merely a correction to the single-configuration picture, but similar to the case of larger etched nanostructures.⁴⁴

XII. COMPARISON WITH EXPERIMENT

In Table II we summarize our results for the different TFQDs considered and experimental results on TFQDs with 10 ML-thick GaAs wetting layers. We give the energy of the main excitonic transition, X^0 , labeled *a*₁ in Fig. 10, the negative trion X^{-1} , labeled *c*₁ in Fig. 10, the trion shift $\Delta(X^0 - X^{-1})$, the singlet-triplet electron-hole exchange splitting δ_0 , the fine-structure splitting of the bright states δ_b , the fine-structure splitting of the dark exciton states δ_d . Our results for the excitonic transition agrees very well with the experimental data where PL is measured around 1.68 eV. The appearance of several peaks in photoluminescence as reported in Ref. 7 is also a feature of our (100,20) TFQD where four excitonic transitions are bright, within an energy window of

5 meV. In order to compare our results with Fig. 4 of Ref. 7 we plotted in Fig. 11 the excitonic transitions of the (100,20) TFQD polarized along the [110] and $[1\bar{1}0]$ directions. The $[1\bar{1}0]$ polarized spectrum has been shifted by 0.1 meV to the blue artificially in order to distinguish both polarizations. We obtain for the first and third and also for several higher energy transitions a polarized signal in agreement with Ref 7. However the fine-structure signal clearly identified in Ref 7 with splittings of 22 to 47 μeV is absent in our calculations. The fine structure of the peaks *a1* and *a2* are given in the insets (c) and (d) of Fig. 11 with splittings of only 2–4 μeV . Peak *a1* is split into two dark states split by 3 μeV from two bright states with different polarizations split themselves further by 4 μeV . Peak *a2* is split into three weakly emitting states arranged in a doublet split by a singlet by 2 μeV and a bright state 4 μeV above. The smaller fine-structure splitting than in self-assembled quantum dots is expected from (i) the fact that the effective extent of the wave functions is larger and (ii) the expectation that the short-range part of electron-hole exchange interaction is proportional to the exciton Bohr radius to the third power would leads to around 30 times larger splittings in InAs than in GaAs (iii) the long-range part of the exchange is expected to be proportional to E_p/E_g^2 , a quantity larger for InAs than GaAs. The striking discrepancy between the experimental evidence and the calculation is unlikely to be related to an overall shape effect and will require further investigations.

The theory gives a trion shift to the red by about 1 meV. While the direction of the shift is according to experiment, its value is clearly underestimated. In Table III we summa-

TABLE V. Compiled reference bulk properties and empirical pseudopotential results for AIAs using the parameters from Table IV.

	LB ^a	Review ^b	LCAO ^{c,d}	GW ^e	Used target	EP results
$\varepsilon(\Gamma_{1v})$			-11.95/-11.87	-12.41	-12.41	-12.53
$\varepsilon(\Gamma_{15v})$	0.0	0.0	0.0	0.0	-6.00	-6.00
$\varepsilon(\Gamma_{1c})$	3.10	3.099	2.79/2.81	2.88	3.10	3.09
$\varepsilon(\Gamma_{15c})$			4.48/4.21	5.14	5.14	4.49
$\varepsilon(X_{1v})$			-9.63/-9.80	-10.41	-10.41	-8.77
$\varepsilon(X_{3v})$	-5.7		-5.69/-5.52	-5.87	-5.70	-7.83
$\varepsilon(X_{5v})$	-2.32		-2.38/-2.32	-2.44	-2.32	-2.34
$\varepsilon(X_{1c})$	2.23	2.24	2.37/2.21	2.14	2.25	2.24
$\varepsilon(X_{3c})$	2.43		3.84/2.89	3.03	2.43	3.02
$\varepsilon(L_{1v})$			-10.28/-10.43	-10.97	-10.97	-10.27
$\varepsilon(L_{2v})$			-5.95/-6.41	-6.01	-6.01	-6.76
$\varepsilon(L_{3v})$			-0.88/-0.97	-3.90	-0.88	-0.95
$\varepsilon(L_{1c})$	2.57	2.46	2.81/2.48	2.91	2.46	2.57
$\varepsilon(L_{3c})$			5.86/4.87	5.59	5.59	5.59
$m_e^*(\Gamma_{1c})$	0.15	0.15			0.15	0.149
$m_e^*(L_{1c,l})$	1.32	1.32				
$m_e^*(L_{1c,t})$	0.15	0.15				
$m_e^*(X_{1c,l})$	1.1	0.97				
$m_e^*(X_{1c,t})$	0.19	0.22				
$m_{hh}^*[100]$	0.51	0.47			0.47	0.40
$m_{hh}^*[111]$	1.09	1.09			1.09	0.90
$m_{lh}^*[100]$	0.18	0.185			0.185	0.161
$m_{lh}^*[111]$	0.15	0.15			0.15	0.13
$a(\Gamma)$	-8.11	-8.11			-8.93	-10.70
$a_v(\Gamma)$	-2.47	-2.47			1.53 ^f	1.47
$a(\Gamma-X)$	1.20				1.01 ^f	0.95
$a(\Gamma-L)$					-4.60 ^f	-4.49
$b[100]$	-2.3	-2.3			-2.3	-2.75
$\Delta_{so}(\Gamma)$	0.275	0.28		0.27	0.275	0.276
$\Delta_{so}(L)$	0.20				0.200	0.180

^aReference 48.

^bReference 49.

^cReference 50.

^dReference 51.

^eReference 52.

^fReference 53.

size experimental results for TFQDs in GaAs wells of different thicknesses. The values obtained experimentally for the negative trion shift for different well width are similar and lie around 3 meV, besides for very thick 50 ML wells where it drops to 1.2 meV. One possible reason for our underestimated trion shifts is the limited amount of correlations we can include in the CI basis due to the limited number of confined levels. This hypothesis is reinforced by the fact that path-integral Monte Carlo calculations^{22,45} where correlations are fully taken into account (while the single-particle Hamiltonian is solved at the effective-mass level) do yield binding energies between 1.5 and 4.0 meV depending on the radius of the monolayer fluctuation (a cylindrical dot was assumed). Our results for the fine-structure splittings is too

low compared to the experimental evidence, as already discussed.

XIII. CONCLUSIONS

We used the atomistic empirical pseudopotential method and configuration interaction to calculate the electronic and optical properties of thickness-fluctuation quantum dots (sometimes called *natural* quantum dots). These structures confined the electron and hole wave function through a single atomic monolayer step in a quantum well. These atomistic calculations require the treatment of up to five million atoms for the largest structure of 100 by 20 nm. We first present results for GaAs/Al_{0.3}Ga_{0.7}As quantum wells where

we quantify the energetic confinement given by the monolayer fluctuation. The in-plane confinement is only few meV but leads to the formation of (1,2,4,4) confined electron states and (1,2,4,4) confined hole states for the (20,20), (40,20), (40,40), and (100,20) TFQDs with 10 ML nominal well thickness, respectively. For quantum wells thicker than 20 ML, no more states are confined inside even our largest dot. For TFQDs with 10 ML nominal thickness, we find wave functions that leak in-plane far beyond the physical dimensions of the dots. The wave function also penetrate significantly out of plane into the $\text{Al}_{0.3}\text{Ga}_{0.7}\text{As}$ barrier and are strongly influenced by its random-alloy fluctuations. The spatial extent of electron and hole states with same index are each irregular but very similar to each other, leading to large overlaps and oscillator strength. A symmetry analysis of the states reveals their strongly dominant heavy-hole character. The calculated optical spectrum for the exciton, biexciton, and both trions show a rich spectrum with several bright transitions. We further demonstrate the strong effect of correlations, leading to states entirely different than the ones given at the single-particle level. Hence, the optical spectrum is strongly affected and becomes generally simpler than at the uncorrelated level. The comparison with experiment is good for the general position of the peaks, the appearance of several transitions, and the polarization of some of them. Some quantitative differences are noticed in the redshift of the biexciton and trions which can be attributed to lack of correlations in the configuration-interaction treatment of such large structures. Also the fine-structure splittings reported in the literature could not be reproduced in the unsegregated and perfectly random structures used in this simulation. The reason for this discrepancy is unlikely to be related to a simple shape effect or the effect of correlations and remains an interesting challenge for further investigations.

ACKNOWLEDGMENTS

We acknowledge financial support from the U.S. Department of Energy, Office of Science, Basic Energy Sciences, under Contract No. DE-AC36-08GO28308 to NREL.

APPENDIX: PSEUDOPOTENTIALS

The pseudopotentials used in this work have been constructed as a sum of Gaussians according to the following analytic expression:

$$v_{\alpha}(q) = \Omega_{\alpha} \sum_{i=1}^4 a_i^{\alpha} e^{-|b_i^{\alpha}|(q - |c_i^{\alpha}|)^2} [1 + f_{\alpha} \text{Tr}(\epsilon)], \quad (\text{A1})$$

where α is an index for the atom type and ϵ the strain tensor. The parameters used for the different atoms are given in Table IV. The kinetic-energy rescaling factor in Eq. (1) was set to 1.1. The nonlocal spin-orbit interaction can be written as^{46,47}

$$\hat{V}_{\text{SO}} = \sum_{i\alpha} \hat{V}_{\alpha}^{\text{SO}}(R_i) = \sum_{i\alpha} \sum_{lm} \lambda_{l,\alpha} V_l^{\text{SO}}(r - R_i) \times |P_{lm}(\mathbf{R}_i)\rangle \mathbf{L} \cdot \mathbf{S} \langle P_{lm}(\mathbf{R}_i)|, \quad (\text{A2})$$

where $|P_{lm}(\mathbf{R}_i)\rangle$ is a projector of angular momentum lm cen-

TABLE VI. Compiled reference bulk properties and empirical pseudopotential results for GaAs using the parameters from Table IV.

Property	LB ^a	Review ^b	GW ^c	Used target	EP results
$\varepsilon(\Gamma_{1v})$	-13.21		-13.03	-13.21	-13.24
$\varepsilon(\Gamma_{15v})$	0.0	0.0	0.0	-5.50	-5.50
$\varepsilon(\Gamma_{1c})$	1.519	1.519	1.52	1.519	1.521
$\varepsilon(\Gamma_{15c})$	4.49		4.61	4.49	4.22
$\varepsilon(X_{1v})$	-10.86		-10.69	-10.86	-10.39
$\varepsilon(X_{3v})$	-6.80		-7.19	-6.80	-7.61
$\varepsilon(X_{5v})$	-2.96		-2.87	-2.96	-2.57
$\varepsilon(X_{1c})$	1.98	1.981	2.01	1.98	1.98
$\varepsilon(X_{3c})$	2.50		2.24	2.50	2.60
$\varepsilon(L_{1v})$	-11.24		-11.41	-11.24	-11.35
$\varepsilon(L_{2v})$	-6.80		-6.97	-6.80	-7.02
$\varepsilon(L_{3v})$	-1.30		-1.28	-1.30	-1.06
$\varepsilon(L_{1c})$	1.81	1.815	1.64	1.81	1.81
$m_e^*(\Gamma_{1c})$	0.067	0.067		0.067	0.064
$m_e^*(L_{1c,l})$	1.9	1.900		1.900	2.180
$m_e^*(L_{1c,t})$	0.19	0.0754		0.0754	0.0766
$m_e^*(X_{1c,l})$	1.80	1.30		1.300	1.301
$m_e^*(X_{1c,t})$	0.257	0.23		0.230	0.237
$m_{hh}^*[100]$	0.400	0.350		0.350	0.346
$m_{hh}^*[111]$	0.57	0.893		0.893	0.824
$m_{hh}^*[100]$	0.082	0.090		0.090	0.085
$a_g(\Gamma)$	-8.4	-8.33		-8.15 ^d	-8.27
$a_v(\Gamma)$	-1.0	-1.16		-1.21 ^d	-1.20
$a(\Gamma-X)$	1.0-2.1			1.05 ^d	2.49
$a(\Gamma-L)$	-2.0			-3.70 ^d	-2.74
$b[100]$	-1.7	-2.0		-2.00	-3.38
$\Delta_{\text{so}}(\Gamma)$	0.341	0.341	0.34	0.341	0.345
$\Delta_{\text{so}}(L)$	0.22			0.22	0.20

^aReference 48.

^bReference 49.

^cReference 52.

^dReference 53.

tered at the atomic position \mathbf{R}_i , \mathbf{L} is the spatial angular-momentum operator, \mathbf{S} is the spin operator with components given by Pauli matrices, and $V_l^{\text{SO}}(r)$ is a potential describing the spin-orbit interaction multiplied with a constant fitting parameter $\lambda_{l,\alpha}$. The functional form of $V_l^{\text{SO}}(r)$ was set to a Gaussian and only the effect of p states ($l=1$) was included.

A compilation of the experimental results for several properties of bulk GaAs and AlAs and the values used as target in the pseudopotential fit as well as the results obtained with the pseudopotentials from Table IV are given in Table V for AlAs and Table VI for GaAs. The band-structure energies are given relative to the VBM [$\varepsilon(\Gamma_{15v})$] besides for $\varepsilon(\Gamma_{15v})$ itself in the ‘‘Used target’’ and ‘‘EP results’’ column where it gives the value used to obtain the accurate band offsets between GaAs and AlAs.

- ¹A. Zrenner, L. V. Butov, M. Hagn, G. Abstreiter, G. Böhm, and G. Weimann, *Phys. Rev. Lett.* **72**, 3382 (1994).
- ²K. Brunner, G. Abstreiter, G. Böhm, G. Tränkle, and G. Weimann, *Phys. Rev. Lett.* **73**, 1138 (1994).
- ³K. Brunner, G. Abstreiter, G. Böhm, G. Tränkle, and G. Weimann, *Appl. Phys. Lett.* **64**, 3320 (1994).
- ⁴H. F. Hess, E. Betzig, T. D. Harris, L. N. Pfeiffer, and K. W. West, *Science* **264**, 1740 (1994).
- ⁵J. Hours, P. Senellart, E. Peter, A. Cavanna, and J. Bloch, *Phys. Rev. B* **71**, 161306(R) (2005).
- ⁶P. Senellart, E. Peter, J. Hours, A. Cavanna, and J. Bloch, *Phys. Rev. B* **72**, 115302 (2005).
- ⁷D. Gammon, E. S. Snow, B. V. Shanabrook, D. S. Katzer, and D. Park, *Phys. Rev. Lett.* **76**, 3005 (1996).
- ⁸E. Ivchenko, *Phys. Status Solidi A* **164**, 487 (1997).
- ⁹S. Gupalov, E. Ivchenko, and A. Kavokin, *J. Exp. Theor. Phys.* **86**, 388 (1998).
- ¹⁰Q. Wu, R. D. Grober, D. Gammon, and D. S. Katzer, *Phys. Rev. B* **62**, 13022 (2000).
- ¹¹J. Guest, T. Stievater, G. Chen, E. Tabak, B. Orr, D. Steel, D. Gammon, and D. Katzer, *Science* **293**, 2224 (2001).
- ¹²D. Gammon, A. L. Efros, T. A. Kennedy, M. Rosen, D. S. Katzer, D. Park, S. W. Brown, V. L. Korenev, and I. A. Merkulov, *Phys. Rev. Lett.* **86**, 5176 (2001).
- ¹³J. G. Tischler, A. S. Bracker, D. Gammon, and D. Park, *Phys. Rev. B* **66**, 081310(R) (2002).
- ¹⁴G. Chen, T. H. Stievater, E. T. Batteh, X. Li, D. G. Steel, D. Gammon, D. S. Katzer, D. Park, and L. J. Sham, *Phys. Rev. Lett.* **88**, 117901 (2002).
- ¹⁵J. Hours, S. Varoutsis, M. Gallart, J. Bloch, I. Robert-Philip, A. Cavanna, I. Abram, F. Laruelle, and J. M. Gerard, *Appl. Phys. Lett.* **82**, 2206 (2003).
- ¹⁶K. Matsuda, T. Saiki, S. Nomura, M. Mihara, Y. Aoyagi, S. Nair, and T. Takagahara, *Phys. Rev. Lett.* **91**, 177401 (2003).
- ¹⁷A. S. Bracker *et al.*, *Phys. Rev. Lett.* **94**, 047402 (2005).
- ¹⁸T. Unold, K. Mueller, C. Lienau, T. Elsaesser, and A. D. Wieck, *Phys. Rev. Lett.* **94**, 137404 (2005).
- ¹⁹J. Berezovsky, O. Gywat, F. Meier, D. Battaglia, X. Peng, and D. Awschalom, *Nat. Phys.* **2**, 831 (2006).
- ²⁰C. Riva, F. M. Peeters, and K. Varga, *Phys. Rev. B* **61**, 13873 (2000).
- ²¹L. C. O. Dacal and J. A. Brum, *Phys. Rev. B* **65**, 115324 (2002).
- ²²A. V. Filinov, C. Riva, F. M. Peeters, Y. E. Lozovik, and M. Bonitz, *Phys. Rev. B* **70**, 035323 (2004).
- ²³S.-S. Li, K. Chang, and J.-B. Xia, *Phys. Rev. B* **71**, 155301 (2005).
- ²⁴P. N. Keating, *Phys. Rev.* **145**, 637 (1966).
- ²⁵A. J. Williamson, L.-W. Wang, and A. Zunger, *Phys. Rev. B* **62**, 12963 (2000).
- ²⁶A. J. Williamson and A. Zunger, *Phys. Rev. B* **59**, 15819 (1999).
- ²⁷L.-W. Wang and A. Zunger, *Phys. Rev. B* **59**, 15806 (1999).
- ²⁸A. Szabo and N. S. Ostlund, *Modern Quantum Chemistry* (McGraw-Hill, New York, 1989).
- ²⁹A. Franceschetti, H. Fu, L.-W. Wang, and A. Zunger, *Phys. Rev. B* **60**, 1819 (1999).
- ³⁰R. Resta, *Phys. Rev. B* **16**, 2717 (1977).
- ³¹S. Guha, A. Madhukar, and K. C. Rajkumar, *Appl. Phys. Lett.* **57**, 2110 (1990).
- ³²D. Bimberg, M. Grundmann, and N. N. Ledentsov, *Quantum Dot Heterostructures* (Wiley, New York, 1999).
- ³³D. Bimberg, F. Heinrichsdorff, R. K. Bauer, D. Gerthsen, D. Stenkamp, D. E. Mars, and J. N. Miller, *J. Vac. Sci. Technol. B* **10**, 1793 (1992).
- ³⁴R. F. Kopf, E. F. Schubert, T. D. Harris, R. S. Becker, and G. H. Gilmer, *J. Appl. Phys.* **74**, 6139 (1993).
- ³⁵V. Savona and W. Langbein, *Phys. Rev. B* **74**, 075311 (2006).
- ³⁶M. Erdmann, C. Ropers, M. Wenderoth, R. G. Ulbrich, S. Malzer, and G. H. Dohler, *Phys. Rev. B* **74**, 125412 (2006).
- ³⁷A. Rudra, E. Pelucchi, D. Oberli, N. Moret, B. Dwir, and E. Kapon, *J. Cryst. Growth* **272**, 615 (2004).
- ³⁸B. Courboules, C. Deparis, J. Massies, M. Leroux, and C. Grattepain, *Appl. Phys. Lett.* **65**, 836 (1994).
- ³⁹G. Bastard, *Wave Mechanics Applied to Semiconductor Heterostructures* (Halstead, New York, 1988).
- ⁴⁰A. G. Norman, M. C. Hanna, P. Dippo, D. H. Levi, R. C. Reedy, J. S. Ward, and M. M. Al-Jassim, in *Proceedings of 31st IEEE Photovoltaic Specialists Conference, Lake Buena Vista, Florida, USA* (IEEE, New York, 2005), pp. 43–48.
- ⁴¹P. Yu and M. Cardona, *Fundamentals of Semiconductors* (Springer, Berlin, 2001).
- ⁴²G. Bester, S. Nair, and A. Zunger, *Phys. Rev. B* **67**, 161306(R) (2003).
- ⁴³L. X. He, G. Bester, and A. Zunger, *Phys. Rev. B* **72**, 195307 (2005).
- ⁴⁴S. Kalliakos, M. Rontani, V. Pellegrini, C. Garcia, A. Pinczuk, G. Goldoni, E. Molinari, L. Pfeiffer, and K. West, *Nat. Phys.* **4**, 467 (2008).
- ⁴⁵A. S. Bracker *et al.*, *Phys. Rev. B* **72**, 035332 (2005).
- ⁴⁶G. Weisz, *Phys. Rev.* **149**, 504 (1966).
- ⁴⁷M. S. Hybertsen and S. G. Louie, *Phys. Rev. B* **34**, 2920 (1986).
- ⁴⁸*Numerical Data and Functional Relationships in Science and Technology*, Landolt-Börnstein, New Series, Group III, Vols. 17, 22, and 41, Pt. A, edited by U. Madelung, M. Schultz, and H. Weiss (Springer-Verlag, Berlin, 1997).
- ⁴⁹I. Vurgaftman, J. R. Meyer, and L. R. Ram-Mohan, *J. Appl. Phys.* **89**, 5815 (2001).
- ⁵⁰M. Huang and W. Y. Ching, *J. Phys. Chem. Solids* **46**, 977 (1985).
- ⁵¹A. Chen and A. Sher, *Phys. Rev. B* **22**, 3886 (1980).
- ⁵²X. Zhu and S. G. Louie, *Phys. Rev. B* **43**, 14142 (1991).
- ⁵³S. H. Wei and A. Zunger, *Phys. Rev. B* **60**, 5404 (1999).